

**Low dissipation of earthquake energy along faults that follow pre-existing weaknesses:
field and microstructural observations of Malawi's Bilila-Mtakataka Fault**

Jack N. Williams^{a,b}, Åke Fagereng^a, Luke N.J. Wedmore^b, Juliet Biggs^b, Hassan Mdala^c,
Felix Mphepo^c, Michael Hodge^a

Affiliations

^a*School of Earth and Environmental Sciences, Cardiff University, Cardiff, UK*

^b*School of Earth Sciences, University of Bristol, Bristol, UK*

^c*Geological Survey Department, Mzuzu Regional Office, Mzuzu, Malawi*

Abstract

Fracturing and gouge formation absorb $\geq 50\%$ of earthquake energy on low displacement (< 1 -
2 km) faults in isotropic crust. To assess how these processes absorb earthquake energy in
anisotropic crust, we performed field and microstructural investigations on the 110 km long,
0.4-1.2 km displacement, Bilila-Mtakataka Fault (BMF), Malawi. Where the fault is parallel
to surface metamorphic fabrics, macroscale fractures define a 5-20 m wide damage zone.
This is narrow relative to where the BMF is foliation-oblique (20-80 m), and to faults with
comparable displacement in isotropic crust (~ 40 -120 m). There is minimal evidence for
cataclasis and microfracturing along the BMF; therefore, despite its 110 km length and
geomorphic evidence for Mw 7-8 earthquakes, widespread fault zone fracturing has not
occurred. We attribute lack of damage to fault growth along shallow and deep-seated pre-
existing weaknesses. This conclusion implies that earthquake energy dissipates differently
along incipient faults in isotropic and anisotropic crust.

Key points

- The Bilila-Mtakataka Fault in Malawi has a narrow (5-20 m) footwall damage zone given its 0.4-1.2 km displacement and 110 km length.
- Gouge formation is limited, and the Bilila-Mtakataka Fault has a low maximum displacement to length ratio.
- Limited fracturing implies earthquakes along pre-existing crustal weaknesses dissipate less energy into fault zones than in intact crust.

Plain language summary

Earthquakes release energy, some of which is radiated as seismic energy to the Earth's surface where it causes ground shaking that poses a risk to human life and infrastructure. However, much of this earthquake energy is also dissipated into the rocks surrounding the fault, which causes them to fracture and fragment. This fracturing process is thought to be particularly prevalent in low displacement (≤ 1 -2 km total displacement) faults as the fault grows by breaking surrounding intact rock. In this study, we demonstrate through field and microscale observations of the Bilila-Mtakataka Fault in southern Malawi that despite its low displacement (0.4-1.2 km) and inferred history of M_w 7-8 earthquakes, only limited fracturing of the surrounding rock has occurred. We propose that this limited fracturing results from earthquakes along the Bilila-Mtakataka Fault that rupture along pre-existing weaknesses in Malawi's crust. If true, then the partitioning of earthquake energy between seismic energy and fracturing in the surrounding crust will be influenced by whether the earthquake is exploiting a pre-existing weakness in the Earth's crust.

1. Introduction

Pre-existing mechanical weaknesses in the crust, such as joints, bedding planes, and metamorphic fabrics can profoundly affect earthquake rupture propagation [Allen, 2005; Hecker *et al.*, 2021; Heermance *et al.*, 2003; Litchfield *et al.*, 2018]. Over multiple earthquake cycles, these weaknesses may therefore influence the progressive development of fault rocks and wall rock fracturing, and thus the ability of faults to transmit fluids [Butler *et al.*, 2008; Crider & Peacock, 2004] and to be detected in geophysical surveys [Kelly *et al.*, 2017]. Furthermore, in continental rifts, normal faults that reactivate well-oriented pre-existing weaknesses can lengthen rapidly at relatively small displacements [Collanega *et al.*, 2019; Hecker *et al.*, 2021; Paton, 2006; Walsh *et al.*, 2002]. Interactions between pre-existing crustal weaknesses and faults can therefore affect seismic hazard [Heermance *et al.*, 2003] and the extent to which fault zone fluid flow can focus minerals into economically viable deposits [Micklethwaite & Cox, 2004].

Fault zone structure is typically described by: (1) one or more relatively narrow ‘fault cores’ that comprise fault breccias, cataclasites, and/or gouges, and can include one or more principal slip zones [Sibson, 1977], and (2) a surrounding ‘damage zone’, where fracture density is high relative to the host rocks but shear displacements are small and the original protolith is preserved [Caine *et al.*, 1996]. Gouge formation and damage zone fracturing can occur in response to quasi-static fault tip propagation [Lockner *et al.*, 1991; Renard *et al.*, 2018] and chemical alteration [Lacroix *et al.*, 2015]. In seismogenic faults, gouges and damage zones also develop when energy released during an earthquake is partially absorbed by rocks surrounding the fault, as described by:

$$E_T = (E_G + E_F) + E_R$$

where E_T is the total earthquake energy release, E_R is radiated seismic energy, and E_G and E_F are the energy required to create a slip surface (fracture energy) and slide along that surface (frictional energy) respectively [Kanamori & Rivera, 2006]. E_G and E_F cannot be distinguished based on geological observations of fault zones; however, together these terms can be considered to represent dissipative processes that reduce the E_R available to reach the surface [Kanamori & Rivera, 2006; McKay et al., 2021; Shipton et al., 2006].

Several lines of evidence suggest that in isotropic crust, fault damage and gouge primarily form during early fault growth. First, a scaling between damage zone width and total fault displacement is only observed for displacements <1-2 km [Savage & Brodsky, 2011; Torabi et al., 2020]. Field observations and particle analysis of gouges also suggest that E_G and E_F account for a much higher proportion of E_T in earthquakes in intact rock ($\geq 50\%$) than in earthquakes along high displacement faults [1-10%; Chester et al., 2005; Wilson et al., 2005]. Finally, damage zone fracturing is particularly prevalent at geometrical complexities [Bistacchi et al., 2010; Childs et al., 2009; Tinti et al., 2005], and these complexities tend to be smoothed as fault accumulates displacement [Sagy et al., 2007].

The structural evolution of faults in anisotropic crust is, however, unclear, with examples of foliation-parallel faults that are relatively narrow [Butler et al., 2008; Heermance et al., 2003; McBeck et al., 2019; Wedmore et al., 2020; Zangerl et al., 2006] or of comparable width [Bistacchi et al., 2010; Soden et al., 2014; Wheeler & Karson, 1989] to a fault with equivalent displacement that cross-cuts foliation or is hosted in isotropic crust. These contrasting observations may reflect variations in confining pressures and temperatures [McBeck et al., 2019; Soden et al., 2014; Williams et al., 2018], relative orientations of the

99 fault, mechanical weakness, and regional principal stresses [*Donath, 1961; Fletcher et al.,*
100 2020; *Misra et al., 2015*], the composition and spacing of fabrics [*Beacom et al., 2001;*
101 *Williams et al., 2018*], and/or the presence of strain-hardening phyllosilicates [*Bistacchi et*
102 *al., 2010; Faulkner et al., 2008*] and mechanically isotropic cataclasite [*Kirkpatrick et al.,*
103 2013]. Therefore, when investigating the structural evolution of faults in anisotropic crust, it
104 is important that the influence of these various factors can be separated.

105
106 Here, we investigate the Bilila-Mtakataka Fault (BMF), a 110 km long normal fault in
107 southern Malawi with geomorphic evidence for Late Quaternary Mw 7-8 earthquakes [*Hodge*
108 *et al., 2018, 2020; Jackson & Blenkinsop, 1997*]. The BMF provides important constraints on
109 near-surface fault zone development in anisotropic crust as it shows variable geometrical
110 relationships with surrounding Proterozoic metamorphic fabrics, and thick sequences of
111 isotropic cataclasite have not developed [*Hodge et al., 2018*]. Furthermore, in the context of
112 normal fault growth models [*Rotevatn et al., 2019; Walsh et al., 2002*], the BMF's 0.4-1.2 km
113 maximum displacement implies it is in its early stages of growth, and field examples of
114 active crustal-scale low-displacement normal fault are comparatively rare [*Biegel & Sammis,*
115 2004; *Gawthorpe & Leeder, 2000*]. Our field and microstructural analyses of the BMF can
116 therefore document the effects of pre-existing anisotropies on earthquake energy dissipation
117 around an incipient but >100 km long normal fault.

118 119 **2. The Bilila-Mtakataka Fault**

120 The BMF is situated in southern Malawi in the amagmatic Makanjira Graben, which geodetic
121 models indicate accommodates ~0.7 mm/yr extension between the San and Rovuma plates near
122 the southern end of the East African Rift's Western Branch [Fig. 1; *Wedmore et al., 2021*]. The
123 BMF is expressed at the surface by an escarpment that juxtaposes Proterozoic Southern

Irumide Belt gneisses in the footwall against hanging wall post-Miocene sediments and, at the 1-10 km scale, follows gently to steeply dipping NW-SE striking amphibolite-granulite facies Southern Irumide Belt metamorphic fabrics [Fig. 1b; *Dawson & Kirkpatrick*, 1968; *Hodge et al.*, 2018; *Jackson & Blenkinsop*, 1997; *Laõ-Dávila et al.*, 2015; *Walshaw*, 1965]. At the base of the escarpment is a continuous 110 km long, 5-28 m high soil-mantled scarp, which on the basis of topographic profiles, is interpreted to have formed in at least two $M_w 7.8 \pm 0.3$ earthquakes, with the most recent event likely occurring within the past 10,000 years [*Hodge et al.*, 2018, 2020]. Variations in scarp height and strike have been used to divide the BMF into six sections (Figs. 1a and b); however, at depths >5 km, these sections may root onto one or two sub-planar weaknesses [*Hodge et al.*, 2018].

The BMF footwall escarpment has a maximum height of ~ 300 m (Fig. 1). Several groundwater boreholes in the BMF hanging wall intersected basement rock at depths <40 m, while others encountered sediments to a maximum drilling depth of 60 m [Fig.1a; *Dawson & Kirkpatrick*, 1968; *Walshaw*, 1965]. Locally, hanging wall basement rock is exposed adjacent to the BMF scarp [*Walshaw*, 1965]. These observations suggest a relatively thin but variable-thickness sequence of post-Miocene sediments in the BMF hanging wall. A conservative upper bound for their thickness is 500 m, which is the thickness of syn-rift sediments across strike of the BMF's northern tip at the southwestern end of Lake Malawi (Fig. 1), and where total regional extension is greater than elsewhere along the BMF [*Scholz et al.*, 2020]. Combining a range of hanging wall sediment thicknesses of 50-500 m with the 300 m high footwall escarpment and an estimated BMF dip of $42-60^\circ$ [*Hodge et al.*, 2018; *Stevens et al.*, 2021], we propose its maximum displacement, D_{max} , is 0.4-1.2 km. Given a fault length (L) of 110 km, the $D_{max}:L$ ratio is $\sim 0.004-0.011$. In the context of normal fault growth models, these observations place the BMF in the initial stages of growth (20-30% of fault lifespan) with

substantial fault lengthening but relatively little displacement [Rotevatn *et al.*, 2019; Walsh *et al.*, 2002].

3. Field and Microstructural Observations

Samples and structural measurements were collected along two rivers oriented approximately perpendicular to the BMF scarp near the villages of Kasinje and Mua (Figs. 1-3, Table S1).

These sites were chosen because they represent locations with fault-parallel and fault-oblique foliations. Microstructural investigations were made with a petrological microscope on thin sections cut perpendicular to a foliation where present. To quantify fracture density in these samples, we measured the length of microfractures in quartz and feldspar grains in three 8-15 mm² regions per sample using FracPaQ v2.2 [Healy *et al.*, 2017], and then divided the total microfracture length by the region's quartzofeldspathic grain area [Wedmore *et al.*, 2020].

Backscatter electron imaging and Energy Dispersive Spectroscopy (EDS) analyses were also performed on selected samples (Table S1) using a Zeiss Sigma HD Field Emission Gun Analytical Scanning Electron Microscope (SEM) in the School of Earth and Environmental Sciences at Cardiff University. Samples were coated with 10 nm of carbon, and the SEM data were acquired with a 15 keV beam energy, 8.9 mm working distance, and 60 µm and 120 µm aperture for point analyses or EDS maps respectively.

Along the ~ 20 km long Mua segment, the BMF scarp is oblique to a gently-dipping curvilinear planar cohesive foliation in biotite gneisses (Fig. 2a). This gneissic foliation is defined by mm-spaced bands of quartz + feldspar alternating with bands of biotite + garnet + hornblende (Fig. S2d). Samples from within 2 m of the 13 m high BMF scarp by the Naminkikowe River, including directly from the scarp itself, contain mm-scale quartzofeldspathic and biotite grains that are locally (15-30% by area) surrounded by a fine-grained (<10 µm grain

size) matrix that consists of fragmented quartzofeldspathic and chlorite grains (Figs. 2, S2, and S3).

At distances 2-20 m from the scarp, a gently NE-dipping set of joints, with a subordinate subvertical N-S striking joint set, is observed in outcrop (Fig. 2c). Joint spacing is 0.01-0.1 m near the fault and increases to >0.1 m at distances 20-350 m from the scarp (Figs. 2c and S2c). In all samples 2-350 m from the BMF scarp at Mua, mm-scale quartzofeldspathic grains are crosscut by microfractures, however, there is no evidence for shear across these microfractures. Microfractures are 1-50 μm thick and contain a brown fine-grained fill identified by qualitative EDS as chlorite and Fe-oxide (Figs. S2 and S4). Microfracture density ($\sim 1\text{-}4\text{ mm}^{-1}$) does not increase with proximity to the fault over our 350 m long transect (Figs. 4 and S2).

Along the $\sim 20\text{-km}$ long Kasinje segment, the BMF is parallel to a foliation defined by quartzofeldspathic bands alternating with bands of hornblende + garnet + biotite (Fig. 3). Adjacent to the 16 m high BMF scarp by the Mtuta River, including in scattered exposure on its immediate hanging wall side, is a 5 m wide interval of fractured rock with 0.1-1 m spaced, foliation-parallel joints (Figs. 3b and S5a). In this macroscopically fractured interval, bands of intact quartzofeldspathic domains and calcite veins are locally interlayered with 10 – 100 μm bands of fragmented plagioclase and calcite (Figs. 3d, S4d, S5b). No macroscopic, fault-related deformation is observed in the hanging wall more than 16 m from the scarp (Figs. 3a and S4f). Samples from this hanging wall section and >5 m into the footwall contain mm-scale quartzofeldspathic grains that are cross-cut by chlorite veins (Figs. S4 and S5). As in the Mua transect, microscale fracture density is $1\text{-}4\text{ mm}^{-1}$ and does not vary systematically along the 80 m long transect (Fig. 4).

4. Bilila-Mtakataka Fault Zone Structure

We now place our field and microstructural observations of the BMF in the context of conceptual fault zone structure models [Caine *et al.*, 1996]. At Mua, we interpret that the fine-grained matrix observed in a 2 m thick cohesive unit adjacent to the scarp (Figs. 2 and S3) formed from grain-scale fragmentation and sliding (i.e., comminution) during slip along the BMF. Evidence for displacement along the BMF is localised within this protocataclasite unit [*sensu* Woodcock & Mort, 2008]. This 2 m wide unit provides a minimum estimate of fault core width at Mua, because the hanging wall is not exposed at this locality (Figs. 2a and 4). We define the BMF footwall damage zone at Mua as the region 2-20 m from the scarp where there is no evidence of grain-scale comminution but relatively closely spaced (0.01-0.1 m) joints are present (Fig. 2c). Although the hanging wall damage zone is not exposed at Mua, it is unlikely to be more than three times wider than the 20 m footwall damage zone [Biegel & Sammis, 2004; Savage & Brodsky, 2011]. Therefore, we suggest that the total width of the damage zone at Mua is 20-80 m.

A near complete footwall to hanging wall section through the BMF is exposed at Kasinje (Fig. 3), however, no distinct gouge or cataclasite layers that would typically define a fault core are observed. We cannot rule out that the lack of a fault core represents incomplete exposure or sampling, although a 2 m thick protocataclasite similar to that observed at Mua should have been clearly visible. We interpret that the full width of the BMF damage zone is contained within the interval of closely spaced foliation-parallel joints that extends ~5 m from the scarp into the footwall, < 16 m into the hanging wall (Fig. 3a) and are not seen outside this interval.

Calcite veins are observed within the damage zone at Kasinje. Calcite is a common alteration product in fault zones elsewhere in Malawi [Williams *et al.*, 2019], and these veins may be linked to precipitation from shallow (depths <5 km) Ca²⁺ rich meteoric waters in Malawi [Dávalos-Elizondo *et al.*, 2021]. Veins at Mua and >5 m from the scarp at Kasinje are dominantly made of Fe-oxide and chlorite; however, the number of these veins is not related to distance to the BMF scarp (Figs. 4, S2, S4, and S5). These minerals are not a common low temperature (<300 °C) alteration product [Tulloch, 1979], nor is dissolved iron typical of hydrothermal fluids in Malawi [Dávalos-Elizondo *et al.*, 2021]. We therefore suggest these veins formed before current rift-related faulting.

Analyses of fault zones are always limited by erosion of incohesive fault rocks and lack of exposure [Shipton *et al.*, 2019]. Nevertheless, at Kasinje the BMF exhibits a composite scarp indicating relatively minor scarp erosion since the most recent BMF earthquake [Hodge *et al.*, 2020]. We also note that incohesive fault rocks are preserved adjacent to fault scarps in similar environments and rock types elsewhere in southern Malawi [Wedmore *et al.*, 2020; Williams *et al.*, 2019] and in other subtropical regions of the East African Rift's Western Branch [Delvaux *et al.*, 2012; Ring, 1994; Vittori *et al.*, 1997; Wheeler & Karson, 1989].

5. Discussion

5.1 Fault damage and the earthquake energy budget

At both Kasinje and Mua, a macroscopic damage zone is observed. Although there is scatter in data compilations, the ratio between fault displacement and damage zone width is typically ~0.1 for faults with comparable displacement (~10²-10³ m) to the BMF [Savage & Brodsky, 2011; Torabi & Berg, 2011]. The 5-20 m wide damage zone at Kasinje, where the BMF is foliation-parallel, is therefore narrow compared to that predicted for a fault with the same

displacement in isotropic crust (40-120 m) and to Mua (20-80 m) where the BMF is foliation-oblique. It follows that when an earthquake on the BMF reactivates near-surface metamorphic foliations, less earthquake energy is dissipated on gouge formation and damage-zone widening (i.e., E_G and E_f in Eq. 1) than if it were propagating through intact rock or across pre-existing weaknesses [Chester *et al.*, 2005; Heermance *et al.*, 2003; Wilson *et al.*, 2005]. Deep-seated (>5 km depth) pre-existing weaknesses may control the BMF's geometry [Hodge *et al.*, 2018; Williams *et al.*, 2019], and so could also contribute to the small release of E_G and E_f during BMF earthquakes. This could account for the lack of increased microfracturing in both the Kasinje and Mua damage zones (Figure 4) compared to the damage zone of a low displacement fault in isotropic crust [Anders & Wiltschko, 1994; Mitchell & Faulkner, 2009].

If less earthquake energy is spent on dissipative processes during earthquake ruptures on the BMF, these ruptures can radiate more seismic energy and host more coseismic slip [Heermance *et al.*, 2003; Kanamori & Rivera, 2006]. This is consistent with relatively large single-event slip/length ratios derived from topographic profiles across the BMF's scarp [Hodge *et al.*, 2020]. Our hypothesis is also supported by studies of continental plate boundary faults, which tend to inherit pre-existing weaknesses and exhibit narrow fault cores relative to their displacement [McKay *et al.*, 2021].

5.2 Implications for fault growth and fault detection in anisotropic crust

Not all faults that follow pre-existing weaknesses exhibit narrow damage zones given their displacement. We suggest that the factors that have facilitated limited wall rock fracturing around the BMF are the favorable orientation of pre-existing weaknesses relative to the regional stresses [Fig. 1a; Hodge *et al.*, 2018; Williams *et al.*, 2019], and that it has yet to

develop thick sequences of mechanically isotropic fault cataclasite and gouges [Kirkpatrick *et al.*, 2013]. The relatively low phyllosilicate content and cohesive nature of the foliation around the BMF [Hodge *et al.*, 2018; Walshaw, 1965], which prevents multiple foliation planes from reactivating, may also have been important in reducing near-surface fault damage [Bistacchi *et al.*, 2010].

It is common to use geophysical techniques such as seismic reflection surveys or fault zone guided waves to investigate the internal structure, mechanics, and extent of active faults [e.g. Ben-Zion, 1998; Cochran *et al.*, 2009; Ellsworth & Malin, 2011; Li *et al.*, 2014]. However, our study of the BMF implies that it may be challenging to image faults in anisotropic crust using these techniques as it will be difficult to distinguish whether seismic velocity contrasts are caused by the limited fault-related fracturing or the pre-existing weakness itself [Gulley *et al.*, 2017; Kelly *et al.*, 2017; Simpson *et al.*, 2020]. In continental rifts that are accumulating synrift sediments, normal faults that reactivate pre-existing weaknesses can be imaged using seismic reflection surveys [Collanega *et al.*, 2019; Phillips *et al.*, 2016; Walsh *et al.*, 2002]. In these cases, pre-existing weaknesses have been proposed to facilitate rapid fault normal lengthening; however, these studies cannot resolve fault structure at scales <10 m. Our findings from the BMF suggest that normal faults with low displacement to length ratios can form relatively narrow damage zones, even when their length is sufficient to crosscut the crust. During their early stages of growth, these faults will therefore be less effective conduits for fluid flow than a fault with equivalent displacement in isotropic rock.

6. Conclusions

Using field and microstructural observations, we find that where southern Malawi's Bilila-Mtakataka Fault (BMF) is parallel to surrounding metamorphic foliations, it has a relatively

narrow damage zone (5-20 m wide), compared to sites where it is foliation-oblique (20-80 m), and to a fault in isotropic crust with comparable displacement [\sim 40-120 m wide for 0.4-1.2 km displacement fault; *Savage & Brodsky, 2011; Torabi & Berg, 2011*]. Minimal evidence for BMF microfracturing and grain comminution is observed regardless of whether the BMF is parallel or oblique to surface foliations.

The general observation of poorly developed fault rocks and a narrow damage zone along the BMF, which is particularly clear where it is parallel to surface fabrics, can be explained if earthquake slip on the BMF reactivates pre-existing weaknesses. These weaknesses are favorably oriented in the regional stress state [*Hodge et al., 2018; Williams et al., 2019*], and we propose reactivation would result in relative little energy being dissipated into accumulating fault gouge and damage [*Kanamori & Rivera, 2006; Wilson et al., 2005*]. This reduction in the amount of dissipative energy is consistent with the high single-event displacement to length ratio of the BMF [*Hodge et al., 2020*]. We suggest that these observations may be applicable to other low-displacement faults that inherit well-oriented pre-existing weaknesses, particularly normal faults in continental rifts. If true, then since less energy is consumed by dissipative processes on these faults, the seismic energy radiated by earthquakes along them will be unusually large.

Acknowledgements

This work is supported by the EPSRC-Global Challenges Research Fund PREPARE (EP/P028233/1) and SAFER-PREPARED (part of the ‘Innovative data services for aquaculture, seismic resilience and drought adaptation in East Africa’ grant; EP/T015462/1) projects. TanDEM-X data were provided through DLR proposal DEM_GEOL0686. Figs. 2c and 3b were provided by Johann Diener. All field data is available via Strabospot

[illegible]

thank Antony Oldroyd and Duncan Muir for assistance with making thin sections and technical assistance with the Scanning Electron Microscope respectively.

References

- Allen, J. L. (2005). A multi-kilometer pseudotachylyte system as an exhumed record of earthquake rupture geometry at hypocentral depths (Colorado, USA). *Tectonophysics*, 402(1-4 SPEC. ISS), 37–54. <https://doi.org/10.1016/j.tecto.2004.10.017>
- Anders, M. H., & Wiltschko, D. V. (1994). Microfracturing, paleostress and the growth of faults. *Journal of Structural Geology*, 16(6), 795–815. [https://doi.org/10.1016/0191-8141\(94\)90146-5](https://doi.org/10.1016/0191-8141(94)90146-5)
- Beacom, L. E., Holdsworth, R. E., McCaffrey, K. J. W., & Anderson, T. B. (2001). A quantitative study of the influence of pre-existing compositional and fabric heterogeneities upon fracture-zone development during basement reactivation. *Geological Society Special Publication*, 186, 195–211. <https://doi.org/10.1144/GSL.SP.2001.186.01.12>
- Ben-Zion, Y. (1998). Properties of seismic fault zone waves and their utility for imaging low-velocity structures. *Journal of Geophysical Research: Solid Earth*, 103(6), 12567–12585. <https://doi.org/10.1029/98jb00768>
- Biegel, R. L., & Sammis, C. G. (2004). Relating Fault Mechanics to Fault Zone Structure. *Advances in Geophysics*, 47(C), 65–111. [https://doi.org/10.1016/S0065-2687\(04\)47002-2](https://doi.org/10.1016/S0065-2687(04)47002-2)
- Bistacchi, A., Massironi, M., & Menegon, L. (2010). Three-dimensional characterization of a crustal-scale fault zone: The Pusteria and Sprechenstein fault system (Eastern Alps).

349 *Journal of Structural Geology*, 32(12), 2022–2041.
350 <https://doi.org/10.1016/j.jsg.2010.06.003>

351 Butler, R. W. H., Bond, C. E., Shipton, Z. K., Jones, R. R., & Casey, M. (2008). Fabric
352 anisotropy controls faulting in the continental crust. *Journal of the Geological Society*,
353 165(2), 449–452. <https://doi.org/10.1144/0016-76492007-129>

354 Caine, J. S., Evans, J. P., & Forster, C. B. (1996). Fault zone architecture and permeability
355 structure. *Geology*, 24(11), 1025–1028.

356 Chester, J. S., Chester, F. M., & Kronenberg, A. K. (2005). Fracture surface energy of the
357 Punchbowl fault, San Andreas system. *Nature*, 437(7055), 133–136.
358 <https://doi.org/10.1038/nature03942>

359 Childs, C., Manzocchi, T., Walsh, J. J., Bonson, C. G., Nicol, A., & Schöpfer, M. P. J.
360 (2009). A geometric model of fault zone and fault rock thickness variations. *Journal of*
361 *Structural Geology*, 31(2), 117–127. <https://doi.org/10.1016/j.jsg.2008.08.009>

362 Cochran, E. S., Li, Y. G., Shearer, P. M., Barbot, S., Fialko, Y., & Vidale, J. E. (2009).
363 Seismic and geodetic evidence for extensive, long-lived fault damage zones. *Geology*,
364 37(4), 315–318. <https://doi.org/10.1130/G25306A.1>

365 Collanega, L., Siuda, K., A.-L. Jackson, C., Bell, R. E., Coleman, A. J., Lenhart, A., et al.
366 (2019). Normal fault growth influenced by basement fabrics: The importance of
367 preferential nucleation from pre-existing structures. *Basin Research*, 31(4), 659–687.
368 <https://doi.org/10.1111/bre.12327>

369 Crider, J. G., & Peacock, D. C. P. (2004). Initiation of brittle faults in the upper crust: A
370 review of field observations. *Journal of Structural Geology*, 26(4), 691–707.
371 <https://doi.org/10.1016/j.jsg.2003.07.007>

372 Dávalos-Elizondo, E., Atekwana, E. A., Atekwana, E. A., Tsokonombwe, G., & Laó-Dávila,
373 D. A. (2021). Medium to low enthalpy geothermal reservoirs estimated from

374 geothermometry and mixing models of hot springs along the Malawi Rift Zone.
375 *Geothermics*, 89. <https://doi.org/10.1016/j.geothermics.2020.101963>

376 Dawson, A. L., & Kirkpatrick, I. M. (1968). The geology of the Cape Maclear peninsula and
377 Lower Bwanje valley. *Bulletin of the Geological Survey, Malawi*, 28.

378 Delvaux, D., Kervyn, F., Macheyeke, A. S., & Temu, E. B. (2012). Geodynamic significance
379 of the TRM segment in the East African Rift (W-Tanzania): Active tectonics and
380 paleostress in the Ufipa plateau and Rukwa basin. *Journal of Structural Geology*, 37,
381 161–180. <https://doi.org/10.1016/j.jsg.2012.01.008>

382 Donath, F. A. (1961). Experimental study of shear failure in anisotropic rocks. *Geological*
383 *Society of America Bulletin*, 72(6), 985–989. [https://doi.org/10.1130/0016-](https://doi.org/10.1130/0016-7606(1961)72[985:ESOSFI]2.0.CO;2)
384 [7606\(1961\)72\[985:ESOSFI\]2.0.CO;2](https://doi.org/10.1130/0016-7606(1961)72[985:ESOSFI]2.0.CO;2)

385 Ellsworth, W. L., & Malin, P. E. (2011). Deep rock damage in the San Andreas Fault
386 revealed by P- and S-type fault-zone-guided waves. In *Fagereng, A., Toy, V.G., and*
387 *Rowland, J. (Eds), Geology of the Earthquake Source: A Volume in Honor of Rick*
388 *Sibson, Geological Society, London, Special Publications.*, 359(1), 39–53.
389 <https://doi.org/10.1144/SP359.3>

390 Faulkner, D. R., Mitchell, T. M., Rutter, E. H., & Cembrano, J. (2008). On the structure and
391 mechanical properties of large strike-slip faults. *Geological Society Special Publication*,
392 299(1), 139–150. <https://doi.org/10.1144/SP299.9>

393 Fletcher, J. M., Teran, O. J., Rockwell, T. K., Oskin, M. E., Hudnut, K. W., Spelz, R. M., et
394 al. (2020). An analysis of the factors that control fault zone architecture and the
395 importance of fault orientation relative to regional stress. *GSA Bulletin*, 1–21.
396 <https://doi.org/10.1130/b35308.1>

397 Gawthorpe, R. L., & Leeder, M. R. (2000). Tectono-sedimentary evolution of active
398 extensional basins. *Basin Research*, 12(3–4), 195–218. <https://doi.org/10.1111/j.1365->

- Gulley, A. K., Eccles, J. D., Kaipio, J. P., & Malin, P. E. (2017). The effect of gradational velocities and anisotropy on fault-zone trapped waves. *Geophysical Journal International*, 210(2), 964–978. <https://doi.org/10.1093/gji/ggx200>
- Healy, D., Rizzo, R. E., Cornwell, D. G., Farrell, N. J. C., Watkins, H., Timms, N. E., et al. (2017). FracPaQ: A MATLAB™ toolbox for the quantification of fracture patterns. *Journal of Structural Geology*, 95, 1–16. <https://doi.org/10.1016/j.jsg.2016.12.003>
- Hecker, S., DeLong, S. B., & Schwartz, D. P. (2021). Rapid strain release on the Bear River fault zone, Utah–Wyoming—The impact of preexisting structure on the rupture behavior of a new normal fault. *Tectonophysics*, 808(March), 228819. <https://doi.org/10.1016/j.tecto.2021.228819>
- Heermance, R., Shipton, Z. K., & Evans, J. P. (2003). Fault structure control on fault slip and ground motion during the 1999 rupture of the Chelungpu fault, Taiwan. *Bulletin of the Seismological Society of America*, 93(3), 1034–1050. <https://doi.org/10.1785/0120010230>
- Hodge, M., Fagereng, A., Biggs, J., & Mdala, H. (2018). Controls on Early-Rift Geometry: New Perspectives From the Bilila-Mtakataka Fault, Malawi. *Geophysical Research Letters*, 45(9), 3896–3905. <https://doi.org/10.1029/2018GL077343>
- Hodge, M., Biggs, J., Fagereng, M., Mdala, H., Wedmore, L. N. J., & Williams, J. N. (2020). Evidence From High-Resolution Topography for Multiple Earthquakes on High Slip-to-Length Fault Scarps: The Bilila-Mtakataka Fault, Malawi. *Tectonics*, 39(2), e2019TC005933. <https://doi.org/10.1029/2019TC005933>
- Jackson, J., & Blenkinsop, T. (1997). The Bilila-Mtakataka fault in Malawi: an active, 100-km long, normal fault segment in thick seismogenic crust. *Tectonics*, 16(1), 137–150. <https://doi.org/10.1029/96TC02494>

424 Kanamori, H., & Rivera, L. (2006). Energy Partitioning During an Earthquake. *Earthquakes:
 425 Radiated Energy and the Physics of Faulting*, 170, 3–13.
 426 <https://doi.org/10.1029/170GM03>

427 Kelly, C. M., Faulkner, D. R., & Rietbrock, A. (2017). Seismically invisible fault zones:
 428 Laboratory insights into imaging faults in anisotropic rocks. *Geophysical Research
 429 Letters*, 44(16), 8205–8212. <https://doi.org/10.1002/2017GL073726>

430 Kirkpatrick, J. D., Bezerra, F. H. R., Shipton, Z. K., Do Nascimento, A. F., Pytharouli, S. I.,
 431 Lunn, R. J., & Soden, A. M. (2013). Scale-dependent influence of pre-existing basement
 432 shear zones on rift faulting: A case study from NE Brazil. *Journal of the Geological
 433 Society*, 170(2), 237–247. <https://doi.org/10.1144/jgs2012-043>

434 Lacroix, B., Tesei, T., Oliot, E., Lahfid, A., & Collettini, C. (2015). Early weakening
 435 processes inside thrust fault. *Tectonics*. <https://doi.org/10.1002/2014TC003716>

436 Lañ-Dávila, D. A., Al-Salmi, H. S., Abdelsalam, M. G., & Atekwana, E. A. (2015).
 437 Hierarchical segmentation of the Malawi Rift: The influence of inherited lithospheric
 438 heterogeneity and kinematics in the evolution of continental rifts. *Tectonics*, 34(12),
 439 2399–2417. <https://doi.org/10.1002/2015TC003953>

440 Li, Y. G., De Pascale, G. P., Quigley, M. C., & Gravley, D. M. (2014). Fault damage zones
 441 of the M7.1 Darfield and M6.3 Christchurch earthquakes characterized by fault-zone
 442 trapped waves. *Tectonophysics*, 618, 79–101. <https://doi.org/10.1016/j.tecto.2014.01.029>

443 Litchfield, N. J., Villamor, P., van Dissen, R. J., Nicol, A., Barnes, P. M., Barrell, D. J. A., et
 444 al. (2018). Surface rupture of multiple crustal faults in the 2016 Mw 7.8 Kaikōura, New
 445 Zealand, earthquake. *Bulletin of the Seismological Society of America*, 108(3B), 1496–
 446 1520. <https://doi.org/10.1785/0120170300>

447 Lockner, D. A., Byerlee, J. D., Kuksenko, V., Ponomarev, A., & Sidorin, A. (1991). Quasi-
 448 static fault growth and shear fracture energy in granite. *Nature*, 350(6313), 39–42.

449 <https://doi.org/10.1038/350039a0>

450 McBeck, J., Mair, K., & Renard, F. (2019). Linking macroscopic failure with

451 micromechanical processes in layered rocks: How layer orientation and roughness

452 control macroscopic behavior. *Tectonophysics*, 750, 229–242.

453 <https://doi.org/10.1016/j.tecto.2018.11.016>

454 McKay, L., Lunn, R. J., Shipton, Z. K., Pytharoulis, S., & Roberts, J. J. (2021). Do intraplate

455 and plate boundary fault systems evolve in a similar way with repeated slip events?

456 *Earth and Planetary Science Letters*, 559, 116757.

457 <https://doi.org/10.1016/j.epsl.2021.116757>

458 Micklethwaite, S., & Cox, S. F. (2004). Fault-segment rupture, aftershock-zone fluid flow,

459 and mineralization. *Geology*, 32(9), 813–816.

460 Misra, S., Ellis, S., & Mandal, N. (2015). Fault damage zones in mechanically layered rocks:

461 The effects of planar anisotropy. *Journal of Geophysical Research: Solid Earth*, 120(8),

462 5432–5452. <https://doi.org/10.1002/2014JB011780>

463 Mitchell, T. M., & Faulkner, D. R. (2009). The nature and origin of off-fault damage

464 surrounding strike-slip fault zones with a wide range of displacements: A field study

465 from the Atacama fault system, northern Chile. *Journal of Structural Geology*, 31(8),

466 802–816. <https://doi.org/10.1016/j.jsg.2009.05.002>

467 Paton, D. A. (2006). Influence of crustal heterogeneity on normal fault dimensions and

468 evolution: southern South Africa extensional system. *Journal of Structural Geology*,

469 28(5), 868–886. <https://doi.org/10.1016/j.jsg.2006.01.006>

470 Phillips, T. B., Jackson, C. A. L., Bell, R. E., Duffy, O. B., & Fossen, H. (2016). Reactivation

471 of intrabasement structures during rifting: A case study from offshore southern Norway.

472 *Journal of Structural Geology*, 91, 54–73. <https://doi.org/10.1016/j.jsg.2016.08.008>

473 Renard, F., Weiss, J., Mathiesen, J., Ben-Zion, Y., Kandula, N., & Cordonnier, B. (2018).

474 Critical Evolution of Damage Toward System-Size Failure in Crystalline Rock. *Journal*
475 *of Geophysical Research: Solid Earth*, 123(2), 1969–1986.
476 <https://doi.org/10.1002/2017JB014964>

477 Ring, U. (1994). The influence of preexisting structure on the evolution of the Cenozoic
478 Malawi rift (East African rift system). *Tectonics*, 13(2), 313–326.
479 <https://doi.org/10.1029/93TC03188>

480 Rotevatn, A., Jackson, C. A. L., Tvedt, A. B. M., Bell, R. E., & Blækkan, I. (2019). How do
481 normal faults grow? *Journal of Structural Geology*, 125, 174–184.
482 <https://doi.org/10.1016/j.jsg.2018.08.005>

483 Sagy, A., Brodsky, E. E., & Axen, G. J. (2007). Evolution of fault surface roughness with
484 slip. *Geology*, 35(3), 283–286. <https://doi.org/10.1130/G23235A.1>

485 Savage, H. M., & Brodsky, E. E. (2011). Collateral damage: Evolution with displacement of
486 fracture distribution and secondary fault strands in fault damage zones. *Journal of*
487 *Geophysical Research: Solid Earth*, 116(3), B03405.
488 <https://doi.org/10.1029/2010JB007665>

489 Scholz, C. A., Shillington, D. J., Wright, L. J. M., Accardo, N., Gaherty, J. B., &
490 Chindandali, P. (2020). Intrarift fault fabric, segmentation, and basin evolution of the
491 Lake Malawi (Nyasa) Rift, East Africa. *Geosphere*, 16(5), 1293–1311.
492 <https://doi.org/10.1130/GES02228.1>

493 Schwanghart, W., & Scherler, D. (2014). Short Communication: TopoToolbox 2 -
494 MATLAB-based software for topographic analysis and modeling in Earth surface
495 sciences. *Earth Surface Dynamics*, 2(1), 1–7. <https://doi.org/10.5194/esurf-2-1-2014>

496 Shipton, Z. K., Evans, J. P., Abercrombie, R. E., & Brodsky, E. E. (2006). The missing sinks:
497 Slip localization in faults, damage zones, and the seismic energy budget. *Geophysical*
498 *Monograph Series*, 170, 217–222. <https://doi.org/10.1029/170GM22>

499 Shipton, Z. K., Roberts, J., Comrie, E., Kremer, Y., Lunn, R., & Caine, J. (2019). Fault
 500 fictions: cognitive biases in the conceptualization of fault zones. *Geological Society*
 501 *Special Publications*.
 502 Sibson, R. H. (1977). Fault rocks and fault mechanisms. *Journal of the Geological Society*,
 503 133(3), 191–213. <https://doi.org/10.1144/gsjgs.133.3.0191>
 504 Simpson, J., Adam, L., van Wijk, K., & Charoensawan, J. (2020). Constraining
 505 Microfractures in Foliated Alpine Fault Rocks With Laser Ultrasonics. *Geophysical*
 506 *Research Letters*, 47(8). <https://doi.org/10.1029/2020GL087378>
 507 Soden, A. M., Shipton, Z. K., Lunn, R. J., Pytharouli, S. I., Kirkpatrick, J. D., Do
 508 Nascimento, A. F., & Bezerra, F. H. R. (2014). Brittle structures focused on subtle
 509 crustal heterogeneities: Implications for flow in fractured rocks. *Journal of the*
 510 *Geological Society*, 171(4), 509–524. <https://doi.org/10.1144/jgs2013-051>
 511 Stevens, V. L., Sloan, R. A., Chindandali, P. R., Wedmore, L. N. J., Salomon, G. W., &
 512 Muir, R. A. (2021). The Entire Crust can be Seismogenic: Evidence from Southern
 513 Malawi. *Tectonics*, 40(6), e2020TC006654. <https://doi.org/10.1029/2020tc006654>
 514 Tinti, E., Spudich, P., & Cocco, M. (2005). Earthquake fracture energy inferred from
 515 kinematic rupture models on extended faults. *Journal of Geophysical Research: Solid*
 516 *Earth*, 110(12), 1–25. <https://doi.org/10.1029/2005JB003644>
 517 Torabi, A., & Berg, S. S. (2011). Scaling of fault attributes: A review. *Marine and Petroleum*
 518 *Geology*. <https://doi.org/10.1016/j.marpetgeo.2011.04.003>
 519 Torabi, A., Ellingsen, T. S. S., Johannessen, M. U., Alaei, B., Rotevatn, A., & Chiarella, D.
 520 (2020). Fault zone architecture and its scaling laws: where does the damage zone start
 521 and stop? *Geological Society, London, Special Publications*, 496(1), 99–124.
 522 <https://doi.org/10.1144/sp496-2018-151>
 523 Tulloch, A. J. (1979). Secondary Ca-Al silicates as low-grade alteration products of granitoid

524 biotite. *Contributions to Mineralogy and Petrology*, 69(2), 105–117.

525 <https://doi.org/10.1007/BF00371854>

526 Vittori, E., Delvaux, D., & Kervyn, F. (1997). Kanda fault: A major seismogenic element
527 west of the Rukwa Rift (Tanzania, East Africa). *Journal of Geodynamics*, 24(1–4), 139–
528 153. [https://doi.org/10.1016/S0264-3707\(96\)00038-5](https://doi.org/10.1016/S0264-3707(96)00038-5)

529 Walsh, J. J., Nicol, A., & Childs, C. (2002). An alternative model for the growth of faults.
530 *Journal of Structural Geology*, 24(11), 1669–1675. [https://doi.org/10.1016/S0191-](https://doi.org/10.1016/S0191-8141(01)00165-1)
531 8141(01)00165-1

532 Walshaw, R. D. (1965). The Geology of the Nchue-Balaka Area. *Bulletin of the Geological*
533 *Survey, Malawi*, 19.

534 Wedmore, L. N. J., Williams, J. N., Biggs, J., Fagereng, Å., Mphepo, F., Dulanya, Z., et al.
535 (2020). Structural inheritance and border fault reactivation during active early-stage
536 rifting along the Thyolo fault, Malawi. *Journal of Structural Geology*, 139, 104097.
537 <https://doi.org/10.1016/j.jsg.2020.104097>

538 Wedmore, L. N. J., Biggs, J., Floyd, M., Fagereng, Å., Mdala, H., Chindandali, P. R. N., et
539 al. (2021). Geodetic constraints on cratonic microplates and broad strain during rifting
540 of thick Southern Africa lithosphere. *Geophysical Research Letters*.

541 Wheeler, W. H., & Karson, J. A. (1989). Structure and kinematics of the Livingstone
542 Mountains border fault zone, Nyasa (Malawi) Rift, southwestern Tanzania. *Journal of*
543 *African Earth Sciences*, 8(2–4), 393–413. [https://doi.org/10.1016/S0899-](https://doi.org/10.1016/S0899-5362(89)80034-X)
544 5362(89)80034-X

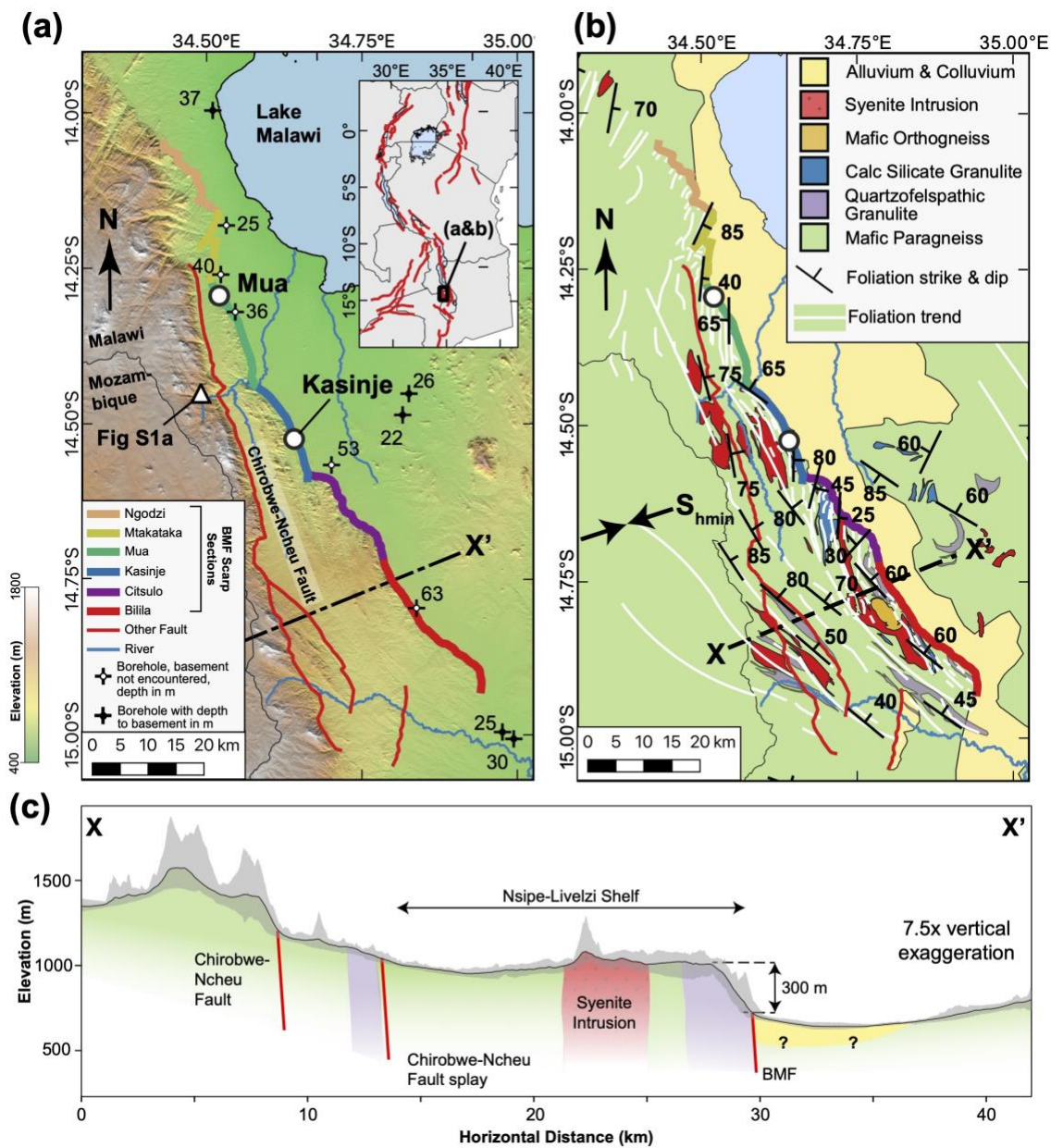
545 Williams, J. N., Toy, V. G., Massiot, C., McNamara, D. D., Smith, S. A. F., & Mills, S.
546 (2018). Controls on fault zone structure and brittle fracturing in the foliated hanging
547 wall of the Alpine Fault. *Solid Earth*, 9(2), 469–489. [https://doi.org/10.5194/se-9-469-](https://doi.org/10.5194/se-9-469-2018)
548 2018

549 Williams, J. N., Fagereng, Å., Wedmore, L. N. J., Biggs, J., Mphepo, F., Dulanya, Z., et al.
550 (2019). How Do Variably Striking Faults Reactivate During Rifting? Insights From
551 Southern Malawi. *Geochemistry, Geophysics, Geosystems*, 20(7), 3588–3607.
552 <https://doi.org/10.1029/2019GC008219>

553 Wilson, B., Dewers, T., Reches, Z., & Brune, J. (2005). Particle size and energetics of gouge
554 from earthquake rupture zones. *Nature*, 434(7034), 749–752.
555 <https://doi.org/10.1038/nature03433>

556 Woodcock, N. H., & Mort, K. (2008). Classification of fault breccias and related fault rocks.
557 *Geological Magazine*, 145(03), 435–440. <https://doi.org/10.1017/S0016756808004883>

558 Zangerl, C., Loew, S., & Eberhardt, E. (2006). Structure, geometry and formation of brittle
559 discontinuities in anisotropic crystalline rocks of the central Gotthard massif,
560 Switzerland. *Eclogae Geologicae Helvetiae*, 99(2), 271–290.
561 <https://doi.org/10.1007/s00015-006-1190-0>
562
563



565

566 Figure 1: Geologic and geomorphic context of the Bilila-Mtakataka Fault (BMF). (a) The six

567 sections of the BMF scarp [Hodge *et al.*, 2018] underlain by a 12 m resolution TanDEM-X

568 digital elevation model, and (b) its surrounding geologic units and foliation orientations

569 [Dawson & Kirkpatrick, 1968; Hodge *et al.*, 2018; Walshaw, 1965]. Inset in (a), the BMF

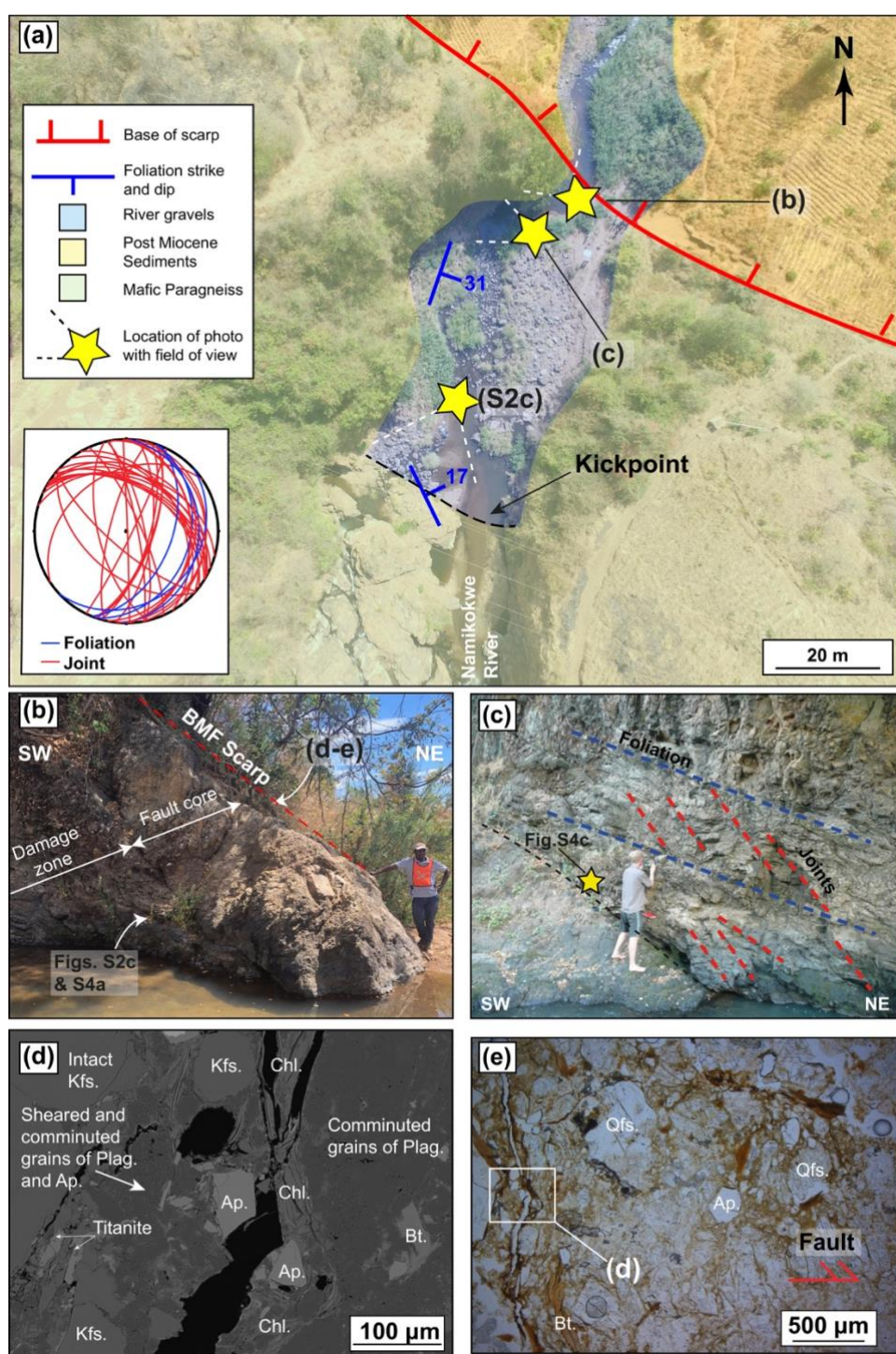
570 location in the context of the East African Rift. Azimuth of minimum horizontal stress (S_{hmin})

571 from a focal mechanism stress inversion [Williams *et al.*, 2019]. (c) Regional scale cross

572 section through the BMF at the point of its maximum footwall relief [Jackson & Blenkinsop,

573 1997], with key as in (b). Black line and shading represent mean and range of topography in a
574 swath 2.5 km either side of the line shown in (a) [*Schwanghart & Scherler, 2014*].

575



577

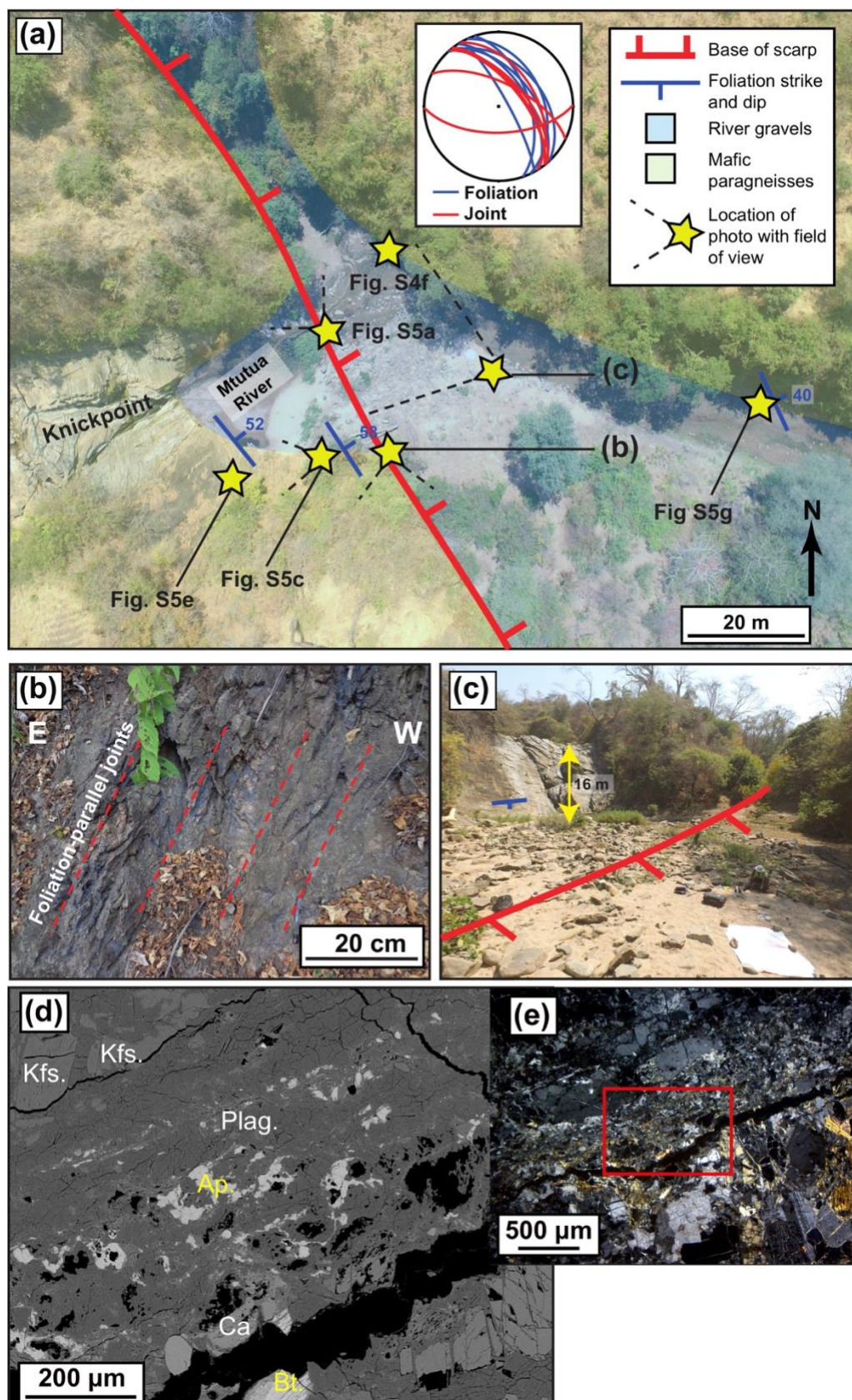
578 Figure 2: Field site at Mua with microstructural observations of BMF-related deformation. (a)

579 Unmanned aerial vehicle (UAV) photograph underlain by geologic/geomorphic units with

580 (inset) equal area stereonet depicting foliation and joint orientations. (b) Exposure adjacent to

581 the BMF scarp, and (c) damage zone at Mua with <0.1 m spaced joints that are oblique to the

582 foliation. (d) Backscatter electron image of thin section from sample adjacent to the BMF
583 scarp with comminuted plagioclase (Plag.) and chlorite (Chl.) grains surrounding K-feldspar
584 (Kfs.) clasts. Mineral identification based on EDS map shown in Fig S3a. Bt.; Biotite, Ap.;
585 Apatite. (e) Photomicrograph in plane polarised light (PPL) of area shown in (d). Qfs,
586 Quartzofeldpathic porphyroclast.



589 Figure 3: Field site at Kasinje with microstructural observations of BMF-related deformation:
590 (a) UAV image of site, (b) BMF damage zone exposure, and (c) oblique view of scarp and
591 knickpoint. (d) Backscattered electron image of fragmented plagioclase (Plag.), calcite (Ca.),
592 and apatite (Ap.) grains from sample adjacent to scarp. Kfs.; K-feldspar, Bt.; Biotite. (e)
593 Photomicrograph of region shown in (d) taken in Cross Polarised Light (XPL).
594

Figure 4

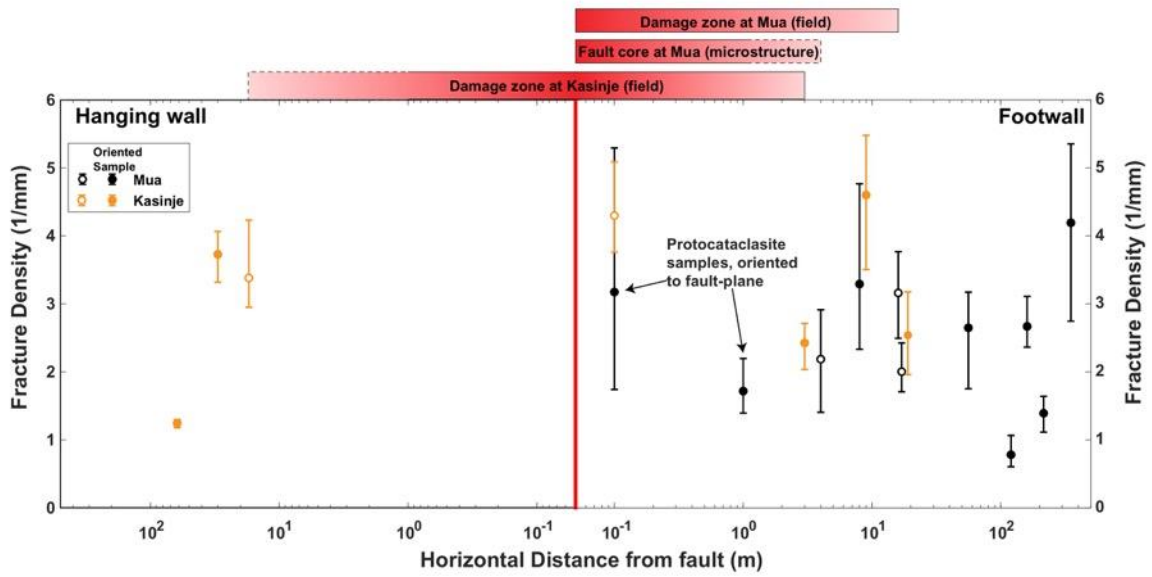


Figure 4: Area-weighted average microscale fracture density in quartz and feldspar grains plotted against horizontal distance from the BMF scarp. Error bars represent the fracture density range over the three sample areas analysed within each thin section. Extent of different fault zone structure components also shown for Mua and Kasinje; lines dashed for where interpretation is based on maximum extent of component due to limited sampling.